IEEE Access
Multidisciplinary | Rapid Review | Open Access Journal

Received July 6, 2017, accepted August 26, 2017, date of publication September 13, 2017, date of current version November 14, 2017.

Digital Object Identifier 10.1109/ACCESS.2017.2751618

Performance Dependence on System Parameters in Millimeter-Wave Active Imaging Based on Complex-Valued Neural Networks to Classify Complex Texture

YUYA ARIMA AND AKIRA HIROSE, (Fellow, IEEE)
Department of Electrical Engineering and Information Systems, The University of Tokyo, Tokyo 113-8656, Japan
Corresponding author: Yuya Arima (y_arima@eis.t.u-tokyo.ac.jp)

This work was supported by JSPS KAKENHI under Grant 21300089.

ABSTRACT Millimeter wave exhibits relatively straight propagation as well as high penetration into dielectric materials, such as plastics, cloth, and paper. In security imaging, we use these features to discover weapons concealed under clothes. Self-organizing map (SOM), a type of neural networks, can map high-dimensional data on any dimension with unsupervised learning. It is utilized for clustering and visualization of high-dimensional data. Previously, we proposed a millimeter-wave imaging system for moving targets consisting of a 1-D array antenna, a parallel front end, and a complex-valued SOM to deal with complex texture. Experiments demonstrated its high performance in the visualization. In this paper, we investigate the dependence of the visualization performance on its configuration parameters as well as processing parameters. We reveal the effect of the modulation-frequency number and the window size. We also discuss the effective depth range for visualization and a tradeoff relationship between the measurement time and the visualization quality.

INDEX TERMS Millimeter wave imaging, neural network, self-organizing feature map, security.

I. INTRODUCTION

There are passive and active schemes in millimeter-wave imaging. Human bodies and things at daily temperature, about 300 K, radiate millimeter and sub-millimeter waves as the so-called black body radiation. Passive imaging detects and images this radiation [1]. Passive imaging is non-coherent, and is similar to photography suitable for obtaining the shape of targets [2]. However, it is sometimes impossible to get sufficient contrast indoors because the power spectrum of the black body radiation depends on the target temperature. Contrarily, active imaging illuminates a target with electromagnetic wave to detect the reflected and/or scattered waves, resulting in sufficient contrast. This fact realizes a quick image acquisition [3]. However, active imaging is affected often by serious noise attributed to its high coherence, called speckle [4]. Though synthetic aperture technology sometimes reduces the impact, the process requires a high calculation cost. Neural networks are also used for high-speed adaptive processing.

Millimeter-wave has straight propagation and high penetration into cloth. Thus, it is potentially applicable to security imaging. Metal detectors have been used in airports. However, because of non-metallic weapons such as resin-made guns, ceramic knives and liquid bombs, some new security measures are expected to develop. Backscatter X-ray full body scanners to image and measure the reflection/scattering, unlike transmission-type X-ray scanners, can be one of the solutions [5]. The amount of emitted X-rays is much less than that from a transmission type, but the influence to the human body is non-negligible. Millimeter-wave presents another solution. It is possible to detect such hazardous materials concealed under clothing by high penetration ability of the millimeter wave [6].

However, existing millimeter-wave body scanners have several problems. One is the fact that passengers have to stop during the scanning. The throughput, therefore, is lower compared with the inspection with conventional metal detectors. Secondly, millimeter-wave systems are mostly expensive mainly because of the high cost required in designing low-loss circuits. Another concern is the privacy. We are able to obtain high-resolution images through the clothes.

To solve these problems, we previously proposed a millimeter-wave imaging system for capturing moving targets consisting of a one-dimensional array antenna and a complex-valued self-organizing map (CSOM) [7], [8]. Since the modulation wavelength is comparable with object size, we are successful in obtaining target shape information. The system utilizes the straight propagation and the high penetration of millimeter wave. CSOM image processing makes it possible to visualize hidden objects by taking the advantages of millimeter wave and envelope phase detection (EPD) processing. It is also possible to realize a high throughput because it is unnecessary for the subjects to stop walking.

In this paper, we investigate the dependence of visualization performance on its configuration parameters as well as processing parameters. We examine the effect of the stepped modulation frequency number and the window size in the system. We also reveal the effective depth for visualization and a trade-off relationship between the measurement interval and the visualization quality. These parameters are important in configuring a practical system.

In Chapter II, we describe an overview of the system, configuration of the actual prototype measurement front-end and the procedure of the image processing. Then, in Chapter III, we conduct experiments to show the effect of configuration and processing parameters on its performance. In Chapter IV, we conduct experiments in another scenario. In Chapter V, we discuss the relationship between the parameters and the performance. Finally, we conclude this paper in Chapter VI.

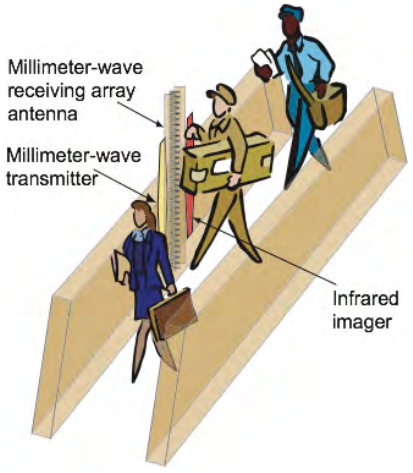

FIGURE 1. Security imaging system for passengers walking through a Shinkansen railway ticket gate.

II. SYSTEM CONSTRUCTION

We propose an active millimeter-wave imaging system to visualize passengers walking through a ticket gate as shown in Fig. 1. It consists of a one-dimensional array antenna and a complex-valued self-organizing map (CSOM). Assumed targets are PET bottles filled with liquid bomb concealed under clothes. We aim at measuring 1,000 people per hour per gate.

It is one of the powerful means to use array antennas to visualize moving targets [9]. In this case, development of low-cost parallel front-end is generally required in order to reduce the cost, which is one of the major challenges of millimeter-wave systems. We present a solution by using our new bulk linearly-tapered slot antenna (bulk LTSA) [10] and envelope phase detection (EPD) [11].

In order to solve the concern for privacy and the scanning time, we use CSOM for adaptive visualization from low-resolution raw images. The CSOM is effective in visualizing plastic landmines buried under ground with our ground penetrating radar (GPR) system [12]–[14]. Since the scattering magnitude from landmines is very close to those from stones, soil and small metal pieces, we have focused on the differences in their complex-amplitude texture in the GPR. This situation is similar to that of passengers. PET bottles filled with liquid bomb have very close value of reflectance to human body. Thus, we focus on phase information and texture of complex amplitude.

The total structure of our proposed system is shown in Fig. 2. The system is composed of a front-end (a transmitting unit and a receiving unit) and an image-processing unit. The system has the following features. The system

1) Measures objects passing in front using sixteen parallel antenna elements.
2) Uses millimeter wave modulated in the amplitude with a sine wave of about 900 MHz for active illumination, and detects the envelope of scattered wave in detection circuits directly connected to the receiving antenna elements.
3) Uses CSOM for image processing to classify targets adaptively even from low resolution data.

Item 1) eliminates the need to stop targets and makes it possible to increase the throughput of the measurement. We need to handle millimeter wave only in the millimeter-wave domain shown in Fig. 2 with the detection circuits described in 2). This configuration reduces the cost by employing low-frequency components (900 MHz), the modulation frequency, in the non-millimeter-wave domain. Item 3) eliminates the need to capture high-resolution data and reduces the privacy issues described above. This unnecessity to capture high-resolution data also contributes to reduction of the measurement time.

Photo of the front end of the measurement unit is shown in Fig. 3. The photo shows a 16-parallel-antenna front end of the receiving unit, a transmitting unit and an optical camera for acquiring sequential one-dimensional image in synchronism with the measurement of the millimeter wave. The use of the bulk-LTSAs, which have a high directivity, as receiving antennas enables us to observe the object as a near field. In other words, the system observes only the front space of the transmitting and receiving antennas, which reduces influence of

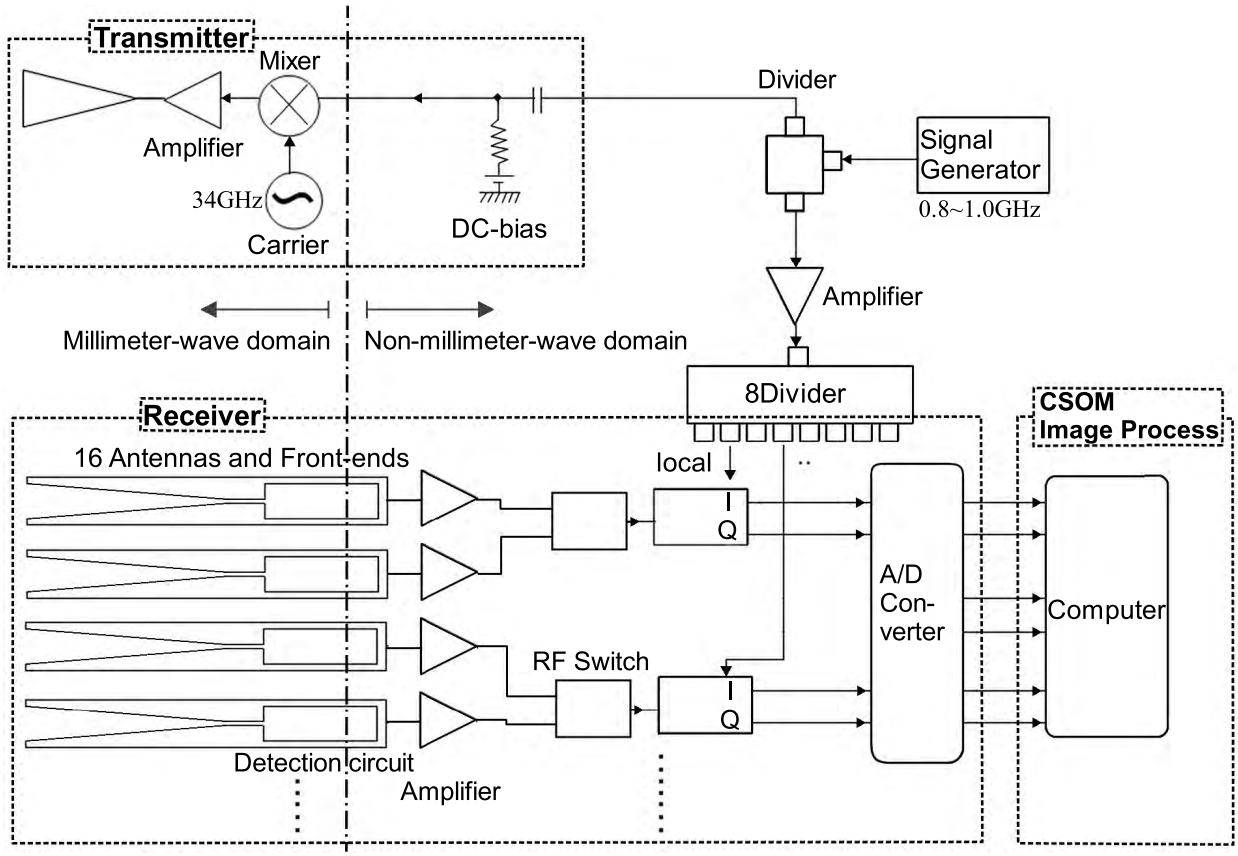

FIGURE 2. Schematic diagram of the millimeter-wave active imaging system consisting of an image-processing unit using a CSOM and a front-end including a one-dimensional array parallel antenna.

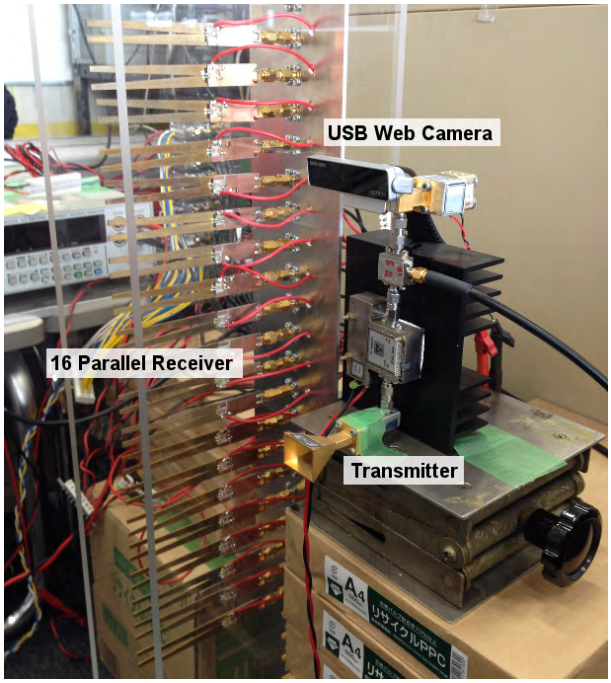

FIGURE 3. Photo of the transmitting unit and the 16-parallel antenna elements of the receiving unit.

surrounding environment. In addition, the unnecessity of the synthetic aperture operation will lead to a reduction of the amount of calculation.

We use 34 GHz millimeter wave generated by a Gunn diode as an illuminating carrier. As shown in Fig. 4, its amplitude is modulated with about 900 MHz sine wave combined with a DC bias. The illumination is transmitted from a horn antenna and scattered by targets. The scattered signal received by the parallel antenna is rectified by the envelope-detection circuits directly connected to the antenna elements. That is, the frequency is converted down to the modulation frequency. Then the signal is homodyne-detected with the local oscillator. The signal is observed as the changes in the phase and amplitude of the modulation frequency wave in this envelope phase detection [11]. Thus, while we utilize the straight propagation and the high penetration of millimeter wave, we can extract human body and plastic bottles by detecting the phase of the modulation wave having a wavelength near to the size of those objects.

The measured data is transferred from the receiving unit to the image-processing unit to be classified by a CSOM. The signal flow of the image processing is shown in Fig. 5. Obtained data is complex amplitude, i.e., phase and amplitude. We calculate complex texture locally to extract feature vectors. We feed the feature vectors to the CSOM to perform classification, and obtain a segmented real-space image colored by the classes. The detail is given below.

We obtain a set of three-dimensional data in the space of antenna elements (L) $\times$ discrete time (T) $\times$ frequencies (N)

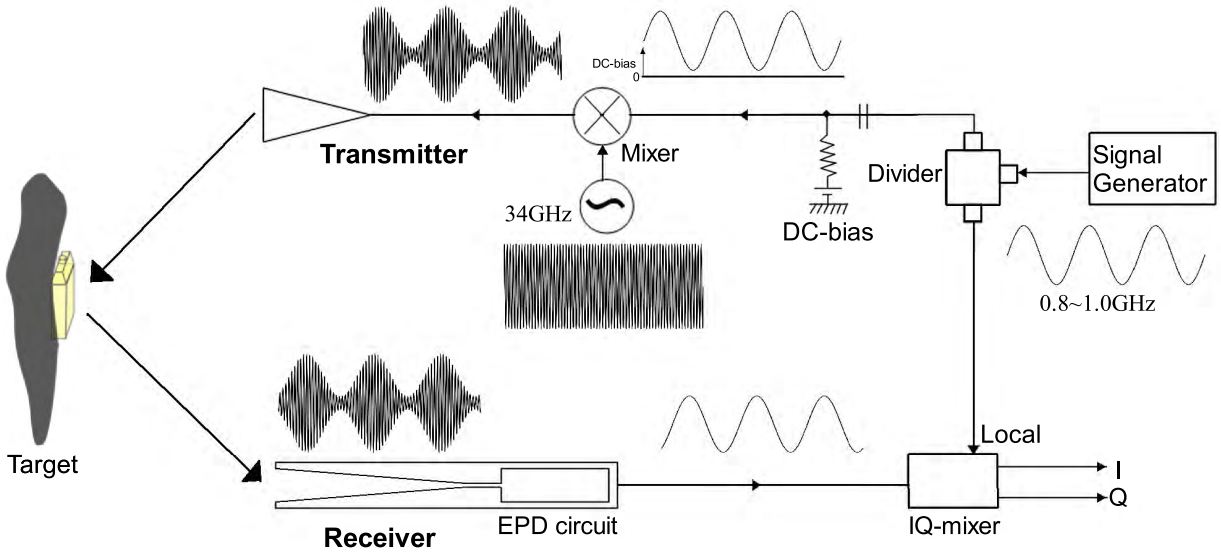

FIGURE 4. Schematic diagram of amplitude modulation for active illumination and envelope phase detection.

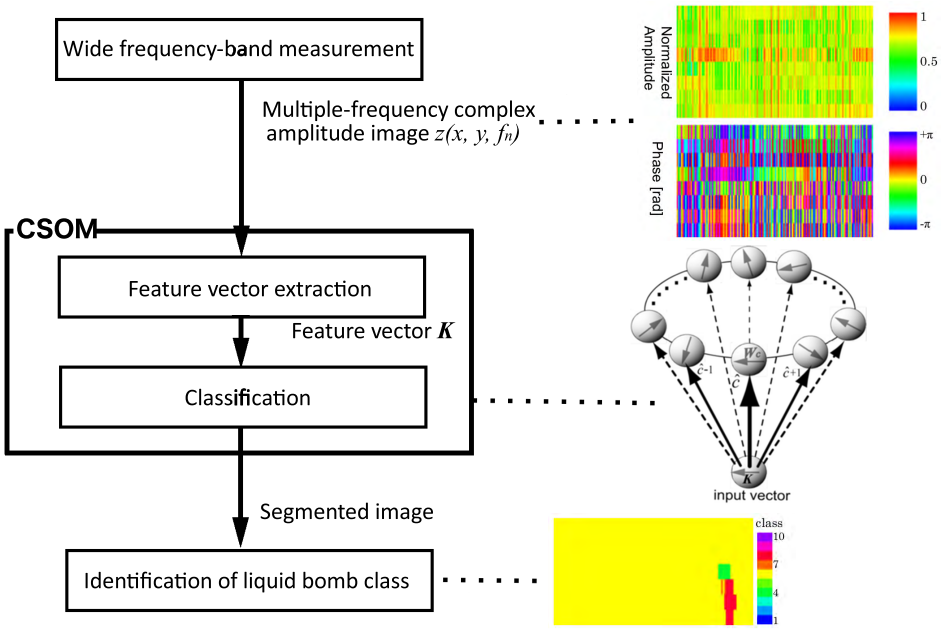

FIGURE 5. Flowchart of image processing.

with high-speed frequency stepped observation. Here, L, T and N denote the number of the elements, the number (length) of discrete time and the number of frequency steps, respectively. We also obtain a set of data without a target z_{coup}, and subtract it from the measured data z_{raw} to mitigate the effects of direct coupling as

$$z(l,t,f_n) = \left(z_{raw}(l,t,f_n) - z_{coup}(l,t,f_n)\right) \cdot \exp(-i\arg(z_{coup}(l,t,f_n))) \quad (1)$$

where a pixel value $z(l,t,f_n)$ means a complex amplitude at the measurement point of antenna element l, discrete time t and modulation frequency f_n.

We extract feature vectors represent local complex texture in a window with a size of $L \times T$. We extract the textural features by calculating correlations among local pixels in real and frequency space. The extraction procedure is as follows. We

i) Cut out a local window of size $L \times T$. (L, T: window size)

ii) Calculate correlation coefficients in the real space $K_s(i, j)$ and the frequency space $K_f(f_n)$ in the local window as feature values as expressed in (4) and (5) in below.

iii) Combine these values and the average value in the local window M in (3) to make a $(N+4)$-dimensional feature vector $\boldsymbol{K}$ in (2).

$$\boldsymbol{K} = \left[M\ K_s(0,0)\ K_s(0,1)\ K_s(1,0)\ K_s(1,1)\right.$$
$$\left. K_f(f_1)\ \ldots\ K_f(f_{N-1})\right]^{\top} \quad (2)$$

$$M = \frac{1}{LTN}\sum_{l=1}^{L}\sum_{t=1}^{T}\sum_{n=1}^{N} z(l,t,f_n) \quad (3)$$

$$K_s(i,j) = \frac{1}{(L-i)(T-j)N}\sum_{l=1}^{L-i}\sum_{t=1}^{T-j}\sum_{n=1}^{N} \times \left\{z^*(l,t,f_n)z(l+i,t+j,f_n)\right\}$$
$$(i,j \in \{0,1\}) \quad (4)$$

$$K_f(f_n) = \frac{1}{LT}\sum_{l=1}^{L}\sum_{t=1}^{T} z^*(l,t,f_n)z(l,t,f_{n+1}) \quad (5)$$

where $(\cdot)^{\top}$ and $(\cdot)^*$ mean transpose and complex conjugate, respectively.

Extracted feature vectors are fed to the CSOM and classified. SOM is a type of neural networks, which is a model of the visual area in the cerebral cortex [15], [16]. The biggest feature of the SOM is the ability to cluster various high-dimensional data without teacher signals. This unsupervised learning is called self-organization. Since our system utilizes the amplitude and phase data, namely the complex amplitude data, we use CSOM (complex-valued SOM), a type of SOM for handling complex-amplitude data [17]. We use a CSOM whose network configuration is a ring to represent the feature-vector similarity in one-dimensional space.

To determine the winner $\hat{c}$ out of the reference vectors, we use the metric based on the complex inner product $\boldsymbol{K}^{\mathrm{H}}\boldsymbol{W_c}$ as

$$\hat{c} = \underset{c}{\operatorname{argmax}}\left(\left|\frac{\boldsymbol{K}^{\mathrm{H}}\boldsymbol{W_c}}{\|\boldsymbol{K}\|\|\boldsymbol{W_c}\|}\right|\right) \ (c : \text{class index}) \quad (6)$$

where $(\cdot)^{\mathrm{H}}$, $|(\cdot)|$ and $\|(\cdot)\|$ means complex conjugate transpose (Hermitian conjugate), absolute value of a complex number and norm of a vector, respectively, and $\boldsymbol{K}$ and $\boldsymbol{W_c}$ denote the input vector for and the reference vector of a

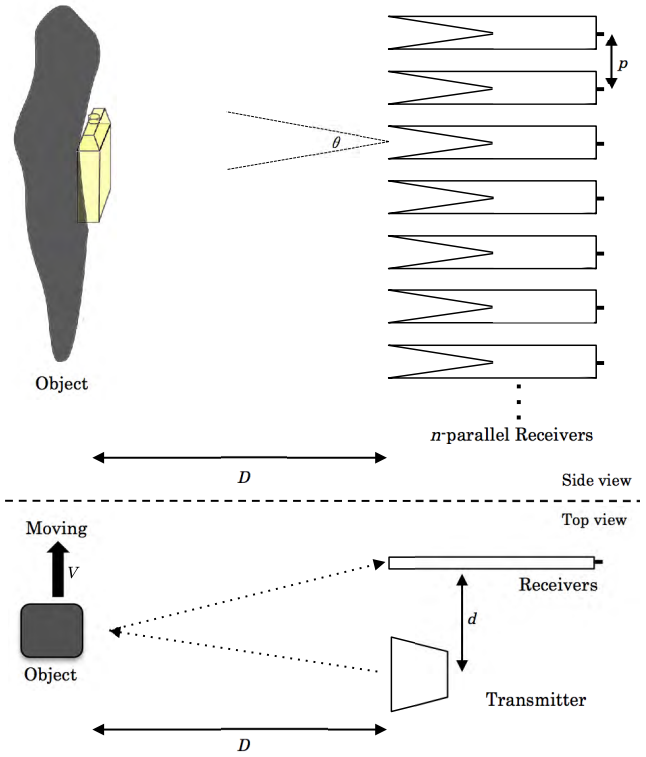

FIGURE 6. Configuration parameters considered in the measurement.

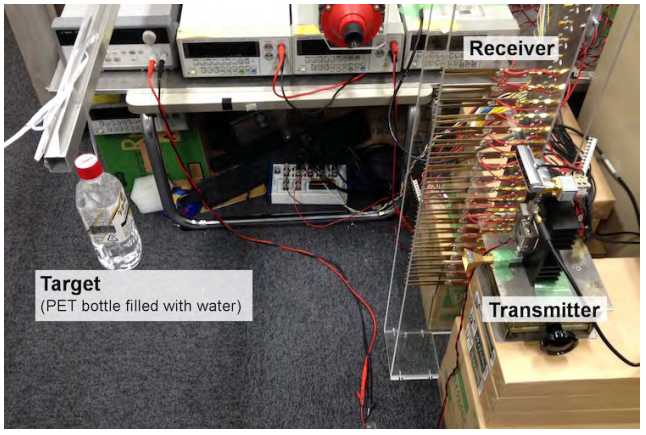

FIGURE 7. Experimental setup targeting a 500mL PET bottle filled with water.

CSOM neuron representing class c defined as

$$\boldsymbol{K} \equiv \begin{bmatrix} r_1\exp(i\theta_1) \\ r_2\exp(i\theta_2) \\ \vdots \end{bmatrix} \quad (7)$$

$$\boldsymbol{W_c} \equiv \begin{bmatrix} q_{c1}\exp(i\psi_{c1}) \\ q_{c2}\exp(i\psi_{c2}) \\ \vdots \end{bmatrix} \quad (8)$$

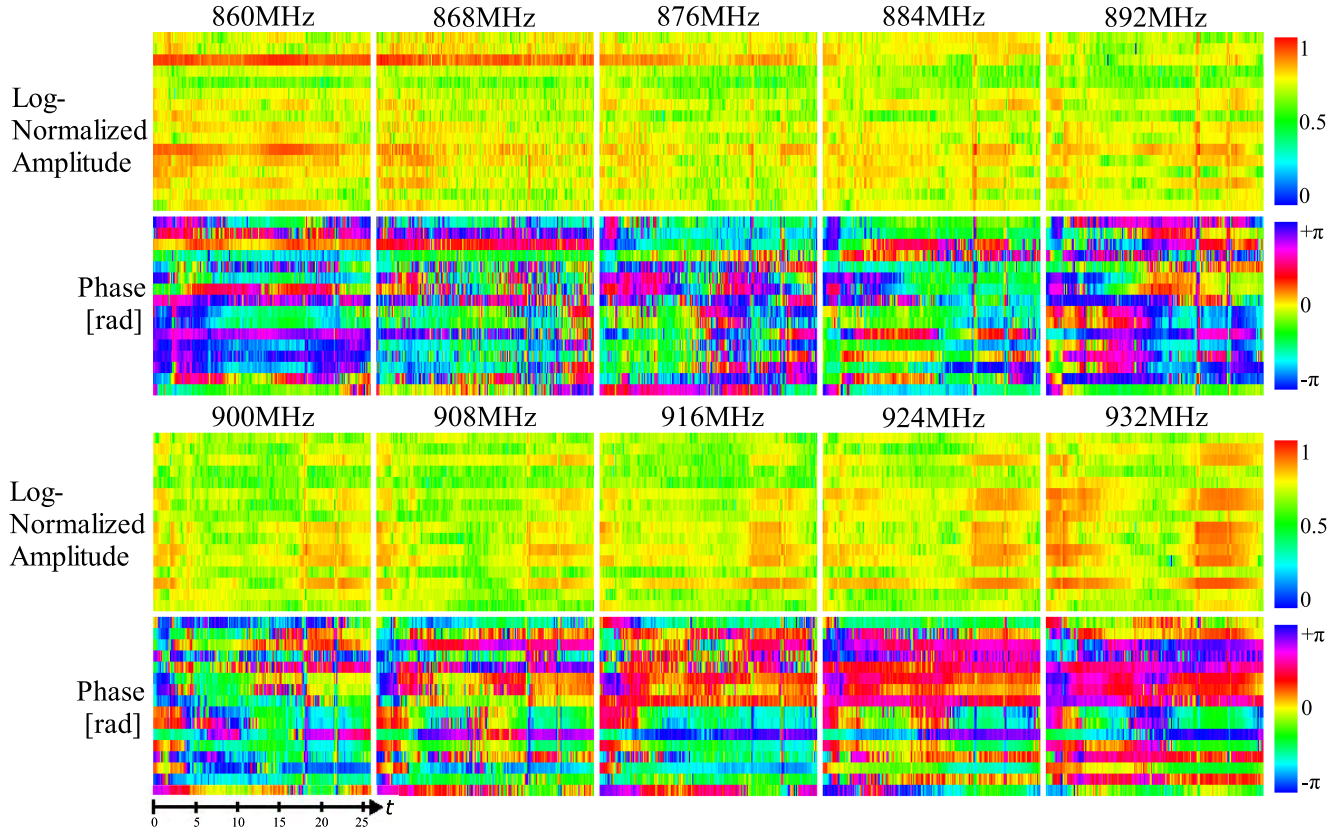

FIGURE 8. Example of captured raw data showing log-normalized amplitude and phase in rad for 10 modulation frequency points with 34 GHz carrier wave.

Then the absolute value of the inner product is expressed as

$$\left|\boldsymbol{K}^{\mathrm{H}}\boldsymbol{W}_{\boldsymbol{c}}\right| = \left|\sum_{j=1}^{N+4}\left[r_j \exp(-i\theta_j)\right]\left[q_{cj}\exp(+i\psi_{cj})\right]\right|$$
$$= \left|\sum_{j=1}^{N+4} r_j q_{cj}\exp(i(\psi_{cj}-\theta_j))\right| \quad (9)$$

The use of a complex inner product makes it possible to perform clustering with more emphasis on phase information than the use of the Euclidean distance [18].

III. EXPERIMENTS

We performed experiments using our proposed system. We measured PET bottles of 500mL filled with water as targets. There are some configuration parameters as shown in Fig. 6 such as directivity of the receiving antenna θ, number of antenna elements n, antenna interval p, distance between the target and the antenna elements D, distance between the transmitter and the receiver d, movement speed of the target V, illumination carrier frequency f_b, modulation frequency (maximum f_H, minimum f_L), number of modulation steps N and scan speed f_s.

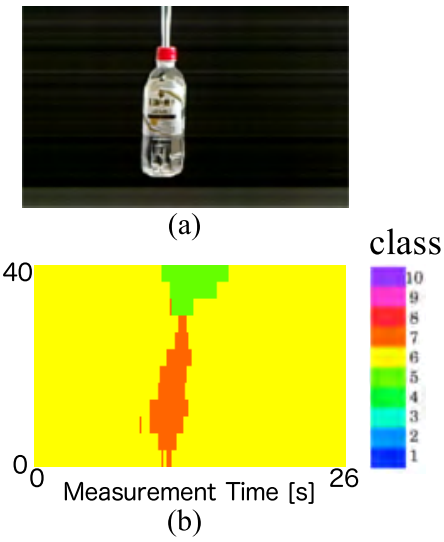

FIGURE 9. (a)Photo of the target synchronized with the measurement and (b)the visualization result by CSOM.

The aim of this experiment is to verify how these configuration parameters effect on the CSOM visualization performance.

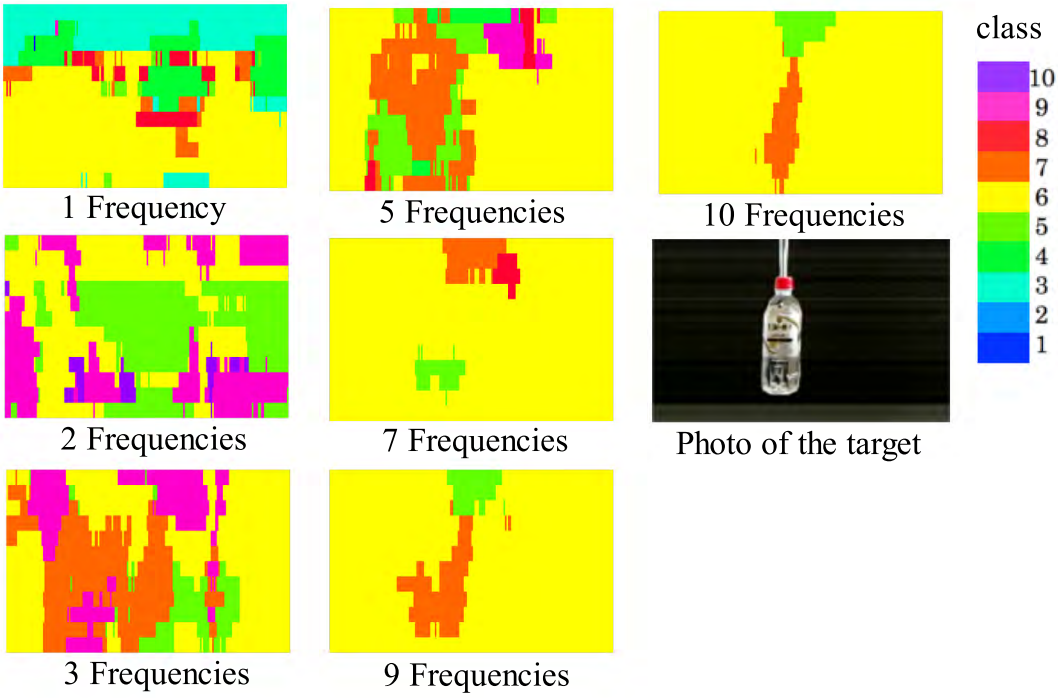

FIGURE 10. Dependence of visualization results on the number of modulation frequency points used for image processing.

A. BASIC EXPERIMENT

The distance D between the antenna elements and the target is about 40 cm and the moving speed of the target V is 2.0 cm/s in this measurement. Measuring time is about 26 s and line scanning frequency f_s is about 7.5 Hz. Scan range is about 36 cm×52 cm. We use 10 points of modulation frequency from 860 MHz to 932 MHz with 8 MHz intervals. Fig. 7 is a picture of the experimental setup. The target object moves to the back direction in this photo. Behind the target, there is a metal rack at approximately 1.1 m from the antennas. We put a radio wave absorber in front of the rack.

Fig. 8 shows an example of the observed raw data as normalized amplitude in dB and phase in rad. Scale of the horizontal direction corresponds to the movement of the object of 2.0 cm/s × 26 s. Note that the data images are left-right reverse to the target view from the antenna side because the obtained data arranged from left to right in chronological order. On the other hand, the scale of the vertical direction is equal to the summation of the height of the antenna element and the gap p, resulting in a total height of Lp. The shape of the target does not appear in the raw data significantly.

Fig. 9 shows a visualization result by the CSOM and an optical image photographing the target from the antenna side. Fig. 9(a) is what we made by cutting out single rows of 1-pixel width from the optical images continuously shooting with the USB web camera in synchronization with the millimeter-wave measurement to be arranged from the left in chronological order. The position of each pixel in the visualization image corresponds to that of the aforementioned raw data, and each color corresponds to each class in the CSOM. We find in their comparison that the area corresponding to the target is divided into classes different from the surrounds. This fact shows that the visualization is successful. Moreover, in order to show the penetration ability of millimeter wave, we placed a thin cloth as a shield in front of the target PET bottle to measure. While the cloth does not appear on the visualization image, the PET bottles were visualized as if there were no shield. We found that the millimeter wave penetrates the cloth effectively. These experiments show that the CSOM works effectively and makes it possible to distinguish the target even from measurement data that we cannot determine the target in raw data.

B. DEPENDENCE OF VISUALIZATION PERFORMANCE ON STEPPED-FREQUENCY PARAMETER

The horizontal resolution of our system is determined in the form of $\frac{V}{f_s}$, where V is the movement speed of the target and f_s is the scanning frequency. Then, it is required to make the scanning frequency higher to accommodate the system for objects moving faster. Measurement time is in substantially proportional to the number of frequency steps because of the time-division multi-frequency observation. Therefore, we intend to reduce the number of frequency steps as far as we obtain sufficient visualization performance. We conducted an experiment and investigated the relationship between the number of frequency steps and the quality of the visualization.

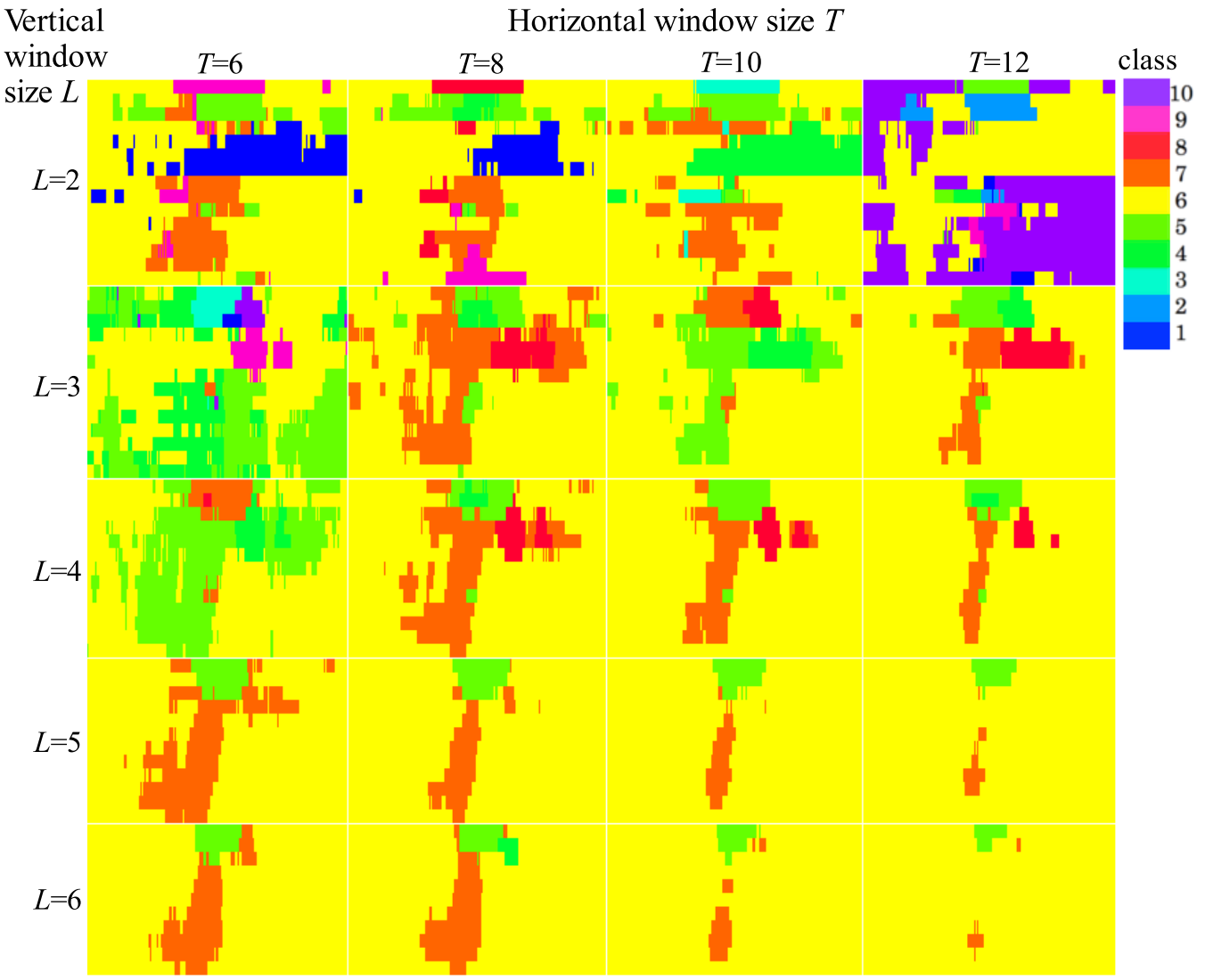

FIGURE 11. Dependence of visualization results on the window size in feature extraction.

In this experiment, we use the data obtained in the previous experiment and generated the visualization results with various numbers of frequency steps by thinning out some frequency data. The result is shown in Fig. 10. In the image using all 10 frequency points, the target is clearly segmented, whereas, in the nine-frequency image, slightly wider area is divided into the class representing a target. Furthermore, in the five-frequency case, the target is divided into a wider range of several classes. Images with even less frequencies no longer distinguish the target.

C. DEPENDENCE OF VISUALIZATION PERFORMANCE ON WINDOW SIZE

To investigate the influence of the window size for extracting a feature vector, the visualization images whose window size (T, L) is changed are shown in Fig. 11. We find that the quality of visualization is very influenced by the window size. Therefore, we examined the factors that determine the optimal window size.

In order to investigate whether the distance between the antenna and the target affects the optimal window size, we put two PET bottles (A and B) at different distance from the antenna as shown in Fig. 12(a). Horizontal distance between the PET bottles is 15 cm, the distance between each of the PET bottles and the antenna is about (A) 30 cm and about (B) 40 cm. Fig. 12(b) is an optical image acquired in synchronization with the measurement of the millimeter wave. Its left and right are reversed from the photo (a) because the obtained data is arranged from the left in chronological order. The visualization results of this measurement data by changing the window size is shown in Fig. 13. PET bottle A, shorter distance from the antenna, is classified well by a small window size, It is clear in particular when $L = 4$ and $T = 10$. On the other hand, PET bottle B, longer distance, is classified when $L = 5$ and $T = 22$, and $L = 6$ and $T = 16$,

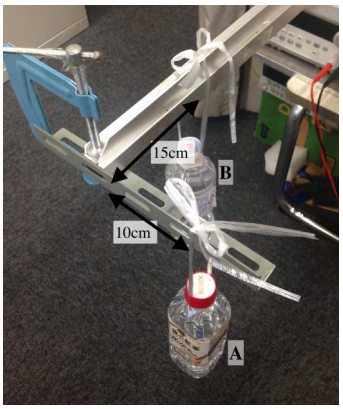

(a)

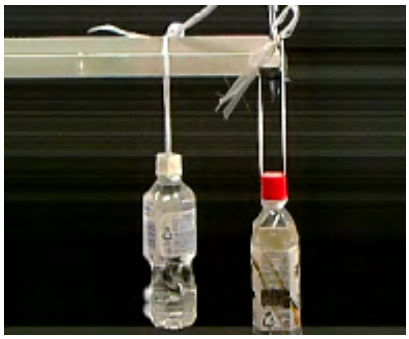

(b)

FIGURE 12. (a)Placement and (b)front view of the measurement of two PET bottles.

but images with a smaller window size are not segmented appropriately. In this way, it has been found that there is an optimal combination between the distance of the target and the antenna and the appropriate window size. The detail is given as follows.

IV. EXPERIMENTS IN ANOTHER SCENARIO

We also conducted experiments in a scenario different from the experiments in Chapter III. In the new experiments, we are targeting a walking person having a 500 mL PET bottle filled with water in his hand. The target pedestrian walks along the white arrow in Fig. 14. We hung a wave absorber of 1 cm thickness at a distance of approximately 90 cm from the antennas beside the pedestrian. Behind the absorber, there are windows about 5 m away, with chairs and tables in between. The subject pedestrian passes through the position of approximately 30 cm from the antennas. The PET bottle is held by his hand in the far side from the antennas. Therefore the distance between the PET bottle and the antennas is approximately 60 cm. We set the walking speed to about 4 cm/s according to the measurement speed of the system to realize a horizontal resolution of about 5 mm. This speed is not constant unlike the previous experiment using the electric stage. The modulation frequencies are set at 10 points with 7 MHz interval from 880 MHz to 943 MHz.

An example of the obtained complex amplitude is shown in Fig. 16. Compared to the optical image shown in Fig. 15, it can be read that the amplitude increases where the pedestrian presents.

The visualization images whose window size (T, L) is changed are shown in Fig. 17. Overall, the tendency that the area of Class 6, which corresponds to the background, spreads as the window size becomes larger, is similar to that seen in the results shown in Fig. 11. If we pay attention to Column $T = 12$, we find that the pedestrian is segmented successfully when $L = 3$ or 4. However, when $L = 6$ or 7, the lower part of the body is not segmented correctly. On the other hand, the PET bottle is segmented when $L = 6$ or $L = 7$ clearly. Next, if we pay attention to the time window size T, the pedestrian is well segmented when T is relatively small, while the PET bottle is segmented successfully with a little longer time window T. Accordingly, we find that there is a correlation between the distance and the effective window size, similar to that found in Section III-C, for visualizing the target in the experiment with different scenario such as target, background and so on.

V. DISCUSSION

A. DEPENDENCE OF VISUALIZATION PERFORMANCE ON STEPPED-FREQUENCY PARAMETER

The experiment showed that, as we use more modulation frequency points to measure, the CSOM performs higher detection quality, and that there is a trade-off relationship between the measurement time and visualization quality. Since our system obtains the changes in the phase by the homodyne detection, the distance from the transmitting antenna to the receiving antenna via the target is contained in the obtained data as phase information. Because the distance information is in fact folded in the range of $[-\pi, \pi]$ for each about 30 cm, the wavelength of the modulation frequency, it has periodic ambiguity. The CSOM processes the multiple-frequency measured data together to solve the ambiguity. In this experiment, it is found that the simple thinning out of the modulation frequency points drops the visualization quality. The measurement with wider frequency range by changing the step size may have potential to maintain visualization quality with less modulation frequency points. In this experiment, the total frequency range is limited by the frequency band of the IQ-mixer (900 MHz $\pm$ 10 %).

B. DEPENDENCE OF VISUALIZATION PERFORMANCE ON WINDOW SIZE

We found that there is some relationship between the distance from the target to the antenna and the optimal window size. We examined what kind of physical nature makes this relationship. In considering the texture of the local area, we assumed that each antenna element measures the scattering at a point in its front. In reality, however, each bulk-LTSA has finite horizontal and vertical directivities θ_h and θ_v as shown Fig.18. Therefore, each antenna element measures with a certain scope. On the other hand, when we attend to one point on the target, we observe the point with multiple antenna elements and over multiple discrete

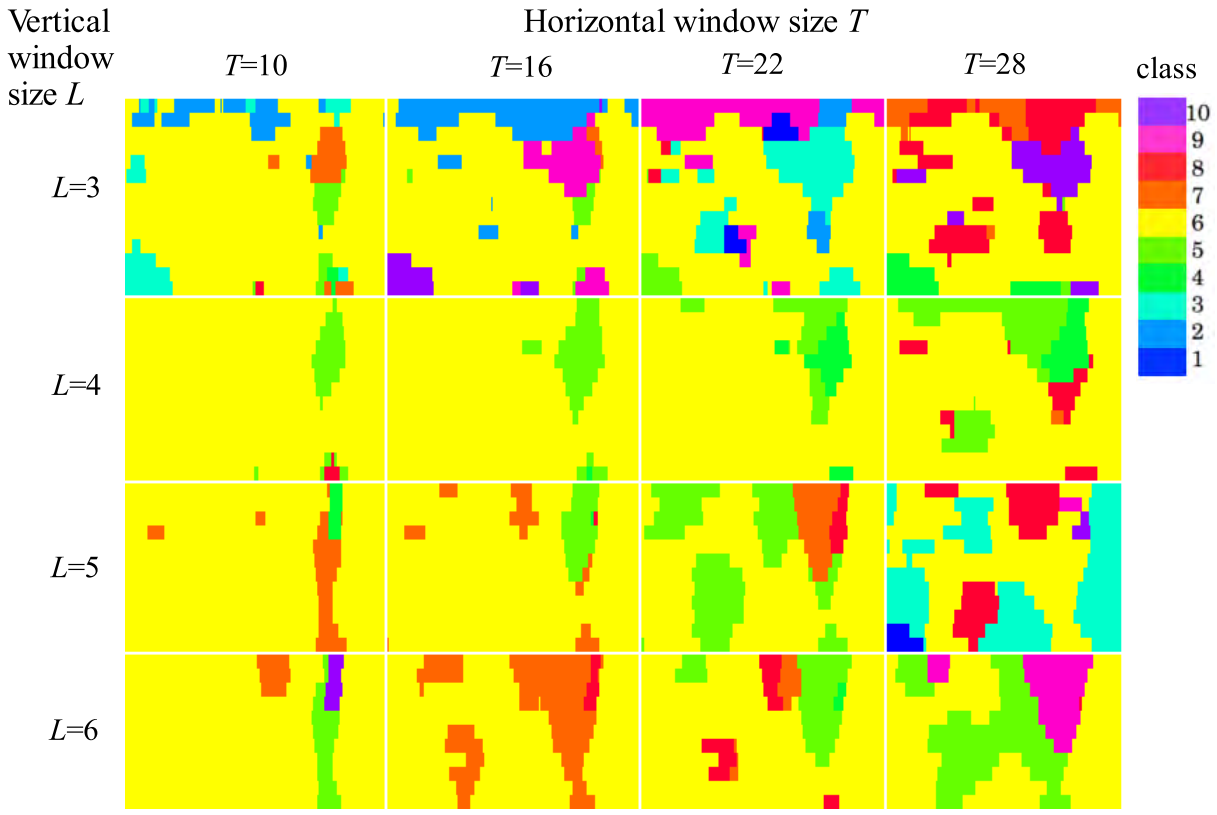

FIGURE 13. Dependence of visualization results on the window size in the measurement of two PET bottles.

FIGURE 14. Experimental setup targeting a walking person. The target walks along the white arrow.

FIGURE 15. Walking person with a 500 mL PET bottle.

time points. Since the number of antenna elements and the time width to observe the target depend on the distance between the target and the antenna D, we can improve the visualization accuracy in the CSOM by setting the window size according to these values. Under this idea, the relationship between the appropriate window size and D can be geometrically derived. The number of antenna elements L to measure the point on the target of distance D should satisfy

$$\frac{(L-1)p}{2\tan\frac{\theta_v}{2}} \leq D < \frac{Lp}{2\tan\frac{\theta_v}{2}} \tag{10}$$

The measurement time width T should also satisfy

$$\frac{VT}{2f_s\tan\frac{\theta_h}{2}} \leq D < \frac{V(T+1)}{2f_s\tan\frac{\theta_h}{2}} \tag{11}$$

where V is the moving speed of the target, f_s is the measuring frequency and T is the time range in which a target point

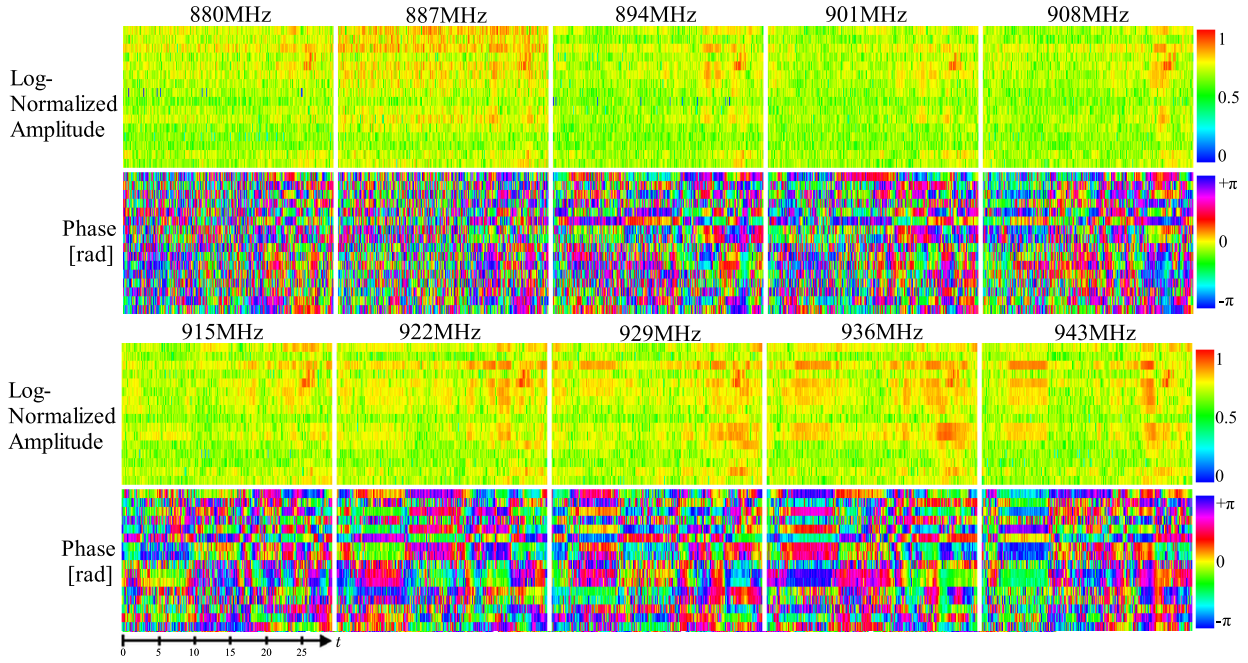

FIGURE 16. Example of captured raw data showing log-normalized amplitude and phase in rad for 10 modulation frequency points with 34 GHz carrier wave.

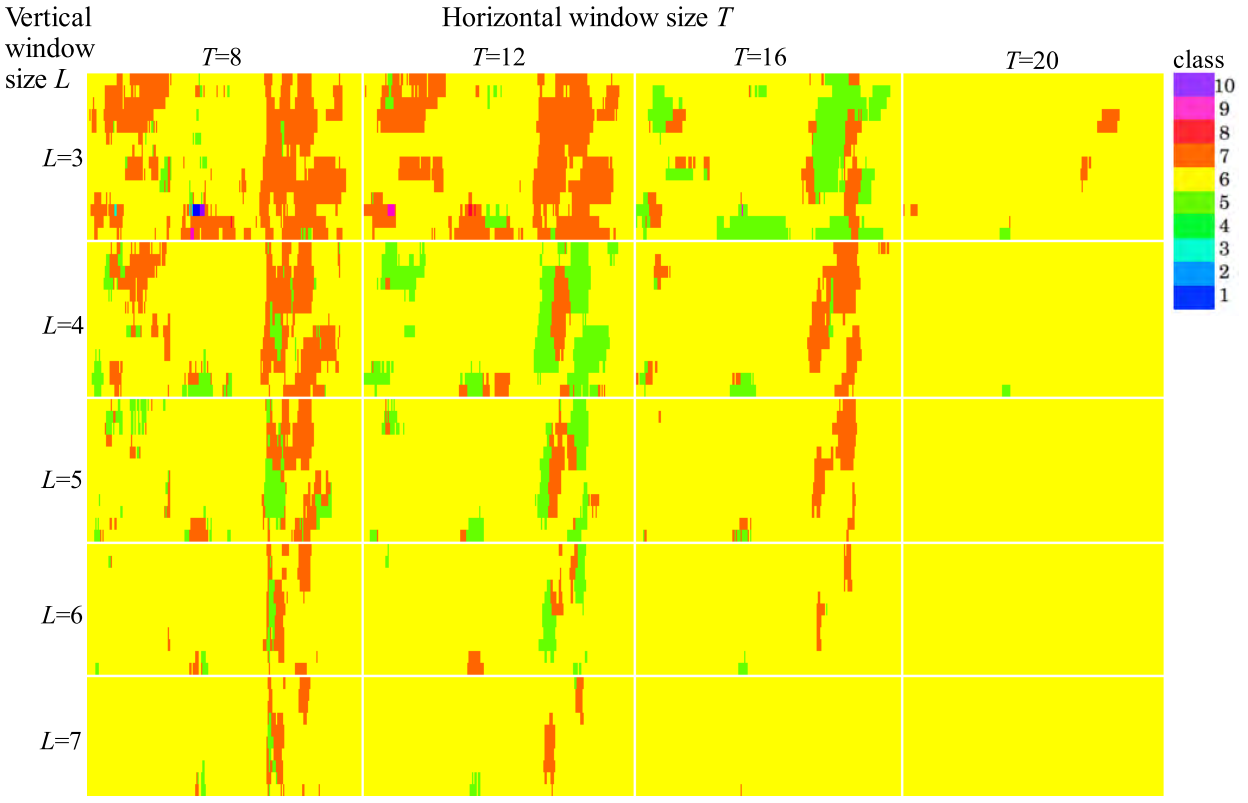

FIGURE 17. Dependence of visualization results on the window size in the measurement of walking person.

exists within the scope of an antenna element. In other words, T and L are determined by the distance D and the antenna directivities θ_h and θ_v.

We consider the examples of the number of antenna elements measuring the target point and the vertical directivity of the antenna. Fig. 19 shows the distance D_L appropriate

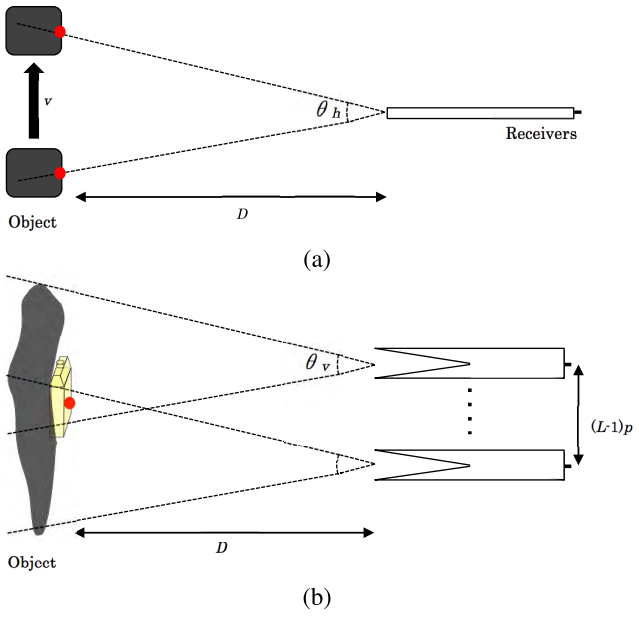

FIGURE 18. Horizontal and vertical measurement scope determined by the directivity of the antenna elements.

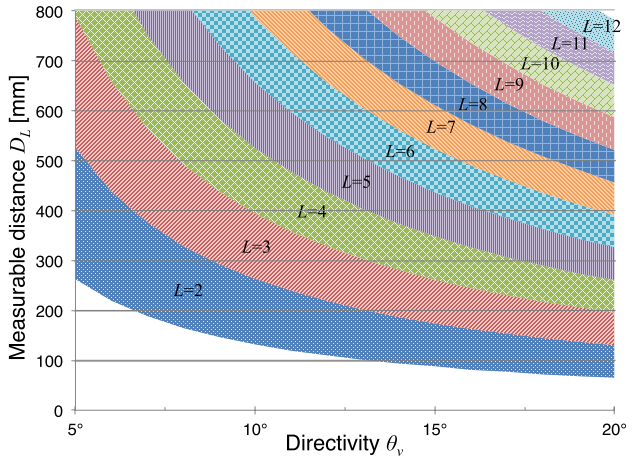

FIGURE 19. The measurable distance D_L for L-antenna elements with vertical directivity of θ_v.

for L elements having a directivity θ_v. From the results shown in Fig. 11, 13 and 17, the value of θ_v is estimated as around 15°. This directivity value is in good agreement with the measurements of the radiation pattern of the bulk LTSA [19]. The experiments showed that the optimal window size depends on the distance of the object. This fact allows more applications focusing on an intended distance by varying the parameters in the feature-extraction process from a single measurement data.

VI. CONCLUSION

In this paper, we evaluated the effect of the configuration parameters and the processing parameters on the visualization performance quantitatively through the experiments, and discussed the reason. In particular, we investigated the effect of the window size in image processing and the number of modulation frequency points for the measurement. As a result, we made clear a trade-off relationship between the sampling frequency and the visualization quality. We also obtained the relationship between the effective depth range of visualization and the processing parameters. These are important findings in configuring a practical system.

REFERENCES

[1] A. I. Sasaki and T. Nagatsuma, "Millimeter-wave imaging using an electrooptic detector as a harmonic mixer," *IEEE J. Sel. Topics Quantum Electron.*, vol. 6, no. 5, pp. 735–740, Sep. 2000.
[2] A. Mizutani, K. Sakakibara, N. Kikuma, and H. Hirayama, "Grating lobe suppression of narrow-wall slotted hollow waveguide millimeter-wave planar antenna for arbitrarily linear polarization," *IEEE Trans. Antennas Propag.*, vol. 55, no. 2, pp. 313–320, Feb. 2007.
[3] V. Tavakol, Q. Feng, I. Ocket, D. Schreurs, and B. Nauwelaers, "System modeling for active mm-wave imaging systems using an enhanced calculation method," in *Proc. IEEE Eur. Radar Conf.*, Oct. 2008, pp. 56–59.
[4] G. Koers *et al.*, "Study of active millimeter-wave image speckle reduction by Hadamard phase pattern illumination," *J. Opt. Soc. Amer. A, Opt. Image Sci. Vis*, vol. 25, no. 2, pp. 312–317, Feb. 2008.
[5] A. Chalmers, "Three applications of backscatter X-ray imaging technology to homeland defense," *Proc. SPIE*, vol. 5778, pp. 989–994, 2005, doi: 10.1117/12.607184.
[6] D. M. Sheen, D. L. McMakin, and T. E. Hall, "Three-dimensional millimeter-wave imaging for concealed weapon detection," *IEEE Trans. Microw. Theory Techn.*, vol. 49, no. 9, pp. 1581–1592, Sep. 2001.
[7] S. Onojima and A. Hirose, "One-dimensional-array millimeter-wave imaging of moving targets for security purpose based on complex-valued self-organizing map (CSOM)," in *Proc. Int. Conf. Neural Inf. Process. (ICONIP)*, Nov. 2012, pp. 229–236.
[8] S. Onojima, Y. Arima, and A. Hirose, "Millimeter-wave security imaging using complex-valued self-organizing map for visualization of moving targets," *Neurocomputing*, vol. 134, pp. 247–253, Jun. 2014.
[9] S. Masuyama and A. Hirose, "Walled LTSA array for rapid, high spatial resolution, and phase-sensitive imaging to visualize plastic landmines," *IEEE Trans. Geosci. Remote Sens.*, vol. 45, no. 8, pp. 2536–2543, Aug. 2007.
[10] D. Radenamad, T. Aoyagi, and A. Hirose, "High-sensitivity millimeter-wave imaging front-end using a low-impedance tapered slot antenna," *IEEE Trans. Antennas Propag.*, vol. 59, no. 12, pp. 4868–4872, Dec. 2011.
[11] A. Hirose, S. Hamada, and R. Yamaki, "Envelope phase detection for millimetre-wave active imaging," *Electron. Lett.*, vol. 45, no. 6, pp. 331–332, Mar. 2009.
[12] T. Hara and A. Hirose, "Plastic mine detecting radar system using complex-valued self-organizing map that deals with multiple-frequency interferometric images," *Neural Netw.*, vol. 17, nos. 8–9, pp. 1201–1210, Nov. 2004.
[13] S. Masuyama, K. Yasuda, and A. Hirose, "Multiple-mode selection of walled-LTSA array elements for high-resolution imaging to visualize antipersonnel plastic landmines," *IEEE Geosci. Remote Sens. Lett.*, vol. 5, no. 4, pp. 745–749, Oct. 2008.
[14] Y. Nakano and A. Hirose, "Taper-walled linearly tapered slot antenna," *IEEE J. Sel. Topics Appl. Earth Observ. Remote Sens.*, vol. 4, no. 4, pp. 779–784, Dec. 2011.
[15] T. Kohonen, *Self-Organization and Associative Memory*, 3rd ed. New York, NY, USA: Springer-Verlag, 1989.
[16] T. Kohonen, *Self-Organizing Maps*. Berlin, Germany: Springer-Verlag, 1995.
[17] A. Hirose, *Complex-Valued Neural Networks*, 2nd ed. Heidelberg, Germany: Springer, 2012.
[18] T. Aoyagi, D. Radenamad, Y. Nakano, and A. Hirose, "Complex-valued self-organizing map clustering using complex inner product in active millimeter-wave imaging," in *Proc. IEEE/INNS Int. Joint Conf. Neural Netw. (IJCNN)*, Jul. 2010, pp. 1346–1351.
[19] D. Radenamad, T. Aoyagi, and A. Hirose, "Low impedance bulk LTSA," *Electron. Lett.*, vol. 46, no. 13, pp. 882–883, Jun. 2010.

YUYA ARIMA received the B.S. degree in electronic and information engineering and the M.S. degree in electrical engineering and information systems from The University of Tokyo, Japan, in 2013 and 2015, respectively, where he is currently pursuing the Ph.D. degree. His research interests include neural networks and millimeter wave radar electronics.

AKIRA HIROSE (F'13) received the Ph.D. degree in electronic engineering from The University of Tokyo in 1991. He is currently a Professor with the Department of Electrical Engineering and Information Systems, The University of Tokyo. His research interests are wireless electronics and neural networks. He is a Senior Member of the IEICE. He served as the President of JNNS from 2013 to 2015 and a Vice President of the IEICE Electronics Society from 2013 to 2015. He served as the Chair of the Neurocomputing Technical Group with the IEICE and the General Chair of the 2013 Asia-Pacific Conference on Synthetic Aperture Radar, Tsukuba. He currently serves as the Founding President of the Asia-Pacific Neural Network Society, the General Chair of the International Conference on Neural Information Processing, Kyoto, in 2016, and the General Chair of International Geoscience and Remote Sensing Symposium, Yokohama, in 2019. He served as an Editor-in-Chief of the *IEICE Transactions on Electronics* from 2011 to 2012 and an Associate Editor of journals, such as the IEEE TRANSACTIONS ON NEURAL NETWORKS from 2009 to 2011 and the *IEEE Geoscience and Remote Sensing Newsletter* from 2009 to 2012.